

Supergranulation is a component of solar convection that manifests itself on the photosphere as a cellular network of around 35 Mm across, with a turnover lifetime of 1–2 days. It is strongly linked to the structure of the magnetic field. The horizontal, divergent flows within supergranule cells carry local field lines to the cell boundaries, while the rotational properties of supergranule upflows may contribute to the restoration of the poloidal field as part of the dynamo mechanism that controls the solar cycle. The solar minimum at the transition from cycle 23 to 24 was notable for its low level of activity and its extended length. It is of interest to study whether the convective phenomena that influences the solar magnetic field during this time differed in character to periods of previous minima. This study investigates three characteristics (velocity components, sizes and lifetimes) of solar supergranulation. Comparisons of these characteristics are made between the minima of cycles 22/23 and 23/24 using MDI Doppler data from 1996 and 2008, respectively. It is found that whereas the lifetimes are equal during both epochs (around 18 h), the sizes are larger in 1996 ( $35.9 \pm 0.3$  Mm) than in 2008 ( $35.0 \pm 0.3$  Mm), while the dominant horizontal velocity flows are weaker ( $139 \pm 1$  m s<sup>-1</sup> in 1996;  $141 \pm 1$  m s<sup>-1</sup> in 2008). Although numerical differences are seen, they are not conclusive proof of the most recent minimum being inherently unusual.

## Comparisons of Supergranule Characteristics During the Solar Minima of Cycles 22/23 and 23/24

Peter E. Williams<sup>1</sup> · W. Dean Pesnell<sup>2</sup>

© Springer ●●●

### 1. Introduction

Studies of the solar cycle are important for understanding hydrodynamic mechanisms within the Sun. They are increasingly being used for making predictions in the long-term about upcoming cycles and in the short-term about evolution of active regions. Such predictions have become important with advances in human technology that can be affected by space weather for which the Sun is ultimately responsible. Studies throughout and comparisons between cycles are vital in constraining these predictions. With the *Solar and Heliospheric Observatory* (SOHO) mission, the opportunity has arisen, for the first time, to make solar observations from a single, space-based instrument through consecutive solar minima. This lays the path for making direct comparisons between adjacent cycles that will assist in prediction making.

---

<sup>1</sup> NASA Postdoctoral Program Fellow,  
Code 671, NASA Goddard Space Flight Center, Greenbelt,  
MD, USA

email: peter.williams@nasa.gov

<sup>2</sup> Code 671, NASA Goddard Space Flight Center, Greenbelt,  
MD, USA

email: william.d.pesnell@nasa.gov

Convection is inextricably linked to processes that determine the behavior of the solar cycle via its interaction with the magnetic field. Internal convective motions induce the lifting and twisting of field lines (the  $\alpha$ -effect) that is at the core of many dynamo models (for example, Käpylä *et al.*, 2006). It is therefore worthwhile to study convective processes to understand their influence on the local magnetic field that may also play a cumulative role in structuring the global field. On the other hand, it is of further interest to understand how convection processes change due to the varying strength of the global field over the course of a solar cycle.

Convection has a variety of components, two well-studied examples being granulation and supergranulation, although the convective nature of the latter is not conclusive. For example, Rieutord *et al.* (2000) have suggested that supergranular flow is generated directly by the granular flow, Beck and Schou (2000), among others, suggest a wave propagation element to supergranulation, while Rast (2003) has proposed that supergranule scales arise through the collective interaction of many small-scale and short-lived granular downflow plumes. Granulation is well resolved in white light observations as bright cellular structures surrounded by dark lanes. They measure about 1 Mm across and have a typical lifetime of around an hour. Their larger counterparts, supergranulation, are typically around 35 Mm across and last for anywhere between 24–48 h. Initially discovered by Hart (1956) as velocity fluctuations over the mean rotation rate, they were first measured using Doppler imaging methods by Leighton *et al.* (1962) which remains a reliable means of observing supergranulation to the present day. Mesogranulation ( $\approx 7$  Mm across) and giant cells ( $\approx 100$  Mm across) have been proposed to exist (November *et al.*, 1981; Simon and Weiss, 1968), but no hard evidence has been forthcoming. It is possible that mesogranulation exists as a combination of small supergranules and large granules, as opposed to a distinct component of convection in itself. Indeed, Hathaway *et al.* (2000) and Rieutord *et al.* (2008) see no appearance of a mesogranulation component

in the power spectra and Matloch *et al.* (2009) suggests that they are a result of the averaging of random data. The direct existence of giant cells has also proved difficult to establish although indirect correlation methods (for example, Beck *et al.*, 1998) have discovered latitudinally-elongated structures that exist over many solar rotations. Giant cells have also been studied via numerical simulations, which may assist in their understanding and direct observation (Miesch *et al.*, 2000; Williams and Cuntz, 2009).

As material from below the photosphere is convected radially upward by the supergranule cells, magnetic field lines are carried along with it. On reaching the surface, the supergranule flow becomes horizontally dominated. This carries the field lines to the edges of the supergranule cell where the field lines are trapped at stagnant points of convergent flow and are forced to advect around the cell boundaries. Supergranulation is observed to be directly linked to the magnetic field via field elements that trace out the boundaries of supergranules clearly seen within, for example, photospheric magnetograms and Ca II K observations of the chromospheric network. H $\alpha$  observations also show these cellular structures, as well as evidence of chromospheric filament material accumulating at the boundaries of supergranules (Pevtsov and Neidig, 2005).

The Michelson Doppler Interferometer (MDI) instrument aboard SOHO (Scherrer *et al.*, 1995) has produced approximately 60-days of full-disk Dopplergrams each year since 1996, thus covering a full solar cycle. Analysis of MDI data has produced a vast array of information about supergranulation such as their evolution (DeRosa and Toomre, 2004), alignment (Lisle *et al.*, 2004) and rotation around the Sun (Meunier and Roudier, 2007) and aided in constraining both numerical simulations of convection (Stein and Nordlund, 2000) and data simulations that produce realistic Dopplergrams by modeling the convection spectrum of MDI (Hathaway *et al.*, 2006).

The most recent solar minimum (*i.e.*, the transition from cycle 23 to 24) has provided much interest due to its extended nature. This has been quantified by

characteristics such as the sunspot number which remained at zero over a period of time unprecedented in the current epoch. Many comparisons between this and previous minima are being made (for example, Howe *et al.*, 2009) to determine whether this minimum stands out as being peculiar.

This work contributes to the comparison between the solar minimum during the transition from cycle 22 to 23, with that from cycle 23 to 24. It uses SOHO/MDI data that covers both periods of interest. It will add to the ongoing study of any peculiarities, as well as the causes and consequences of the 23/24 minimum. By studying supergranule characteristics during both epochs, changes in the convection zone that reflect the differences in the behavior of the magnetic field at these two times may be quantified.

## 2. Data Preparation

A popular method of studying supergranule convection flows is through the use of Dopplergrams. In recent years, these have been predominantly delivered by MDI upon SOHO. MDI has produced yearly Dynamics Runs of approximately 60-days worth of  $1024 \times 1024$  pixel Dopplergrams at a 1-min cadence. For this study, 62 days of data from 1996 (MDI Day 1239-1300; 24 May 24 1996 - 24 July 1996) and 60 days from 2008 (MDI Day 5540-5599; 3 March 2008 - 1 May 2008), both during a period of solar minimum, are used.

To extract convective kinematic characteristics, the Dopplergrams have been reduced to isolate the line-of-sight velocities of surface convection cells. From these, a variety of analysis techniques are used to determine values for the horizontal and radial velocity components of supergranules, their spatial sizes and their  $1/e$  lifetimes, and to provide inter-year comparisons.

A number of independent velocity signals need to be removed from each Dopplergram to extract supergranule flow velocities. First to be removed are the velocities arising due to 5-min p-mode oscillations (Hathaway, 1988). A

31-min temporal Gaussian filter, with an FWHM of 8 min, is constructed to produce a weighted average of a set of 31 1-min Dopplergrams. Each component Dopplergram is de-rotated to match the convection pattern with that of the central Dopplergram within the filter. The resultant time-series is sampled every 15 min, producing a set of 96 averaged Dopplergrams per day.

After subtracting the gravitational redshift and velocity signals due to the motion of the observer, each averaged Dopplergram undergoes further reduction with the removal of the axisymmetric flows (Hathaway, 1987, 1992). Fits are produced for the velocity fields relating to the differential rotation, meridional circulation and convective blueshift due to unresolved convection components, that are subsequently subtracted from the Dopplergrams. The resulting velocity images contain only the line-of-sight velocity fields at the photosphere which may be displayed either in heliocentric or heliographic coordinate systems depending on the analysis.

During the removal of the aforementioned velocity fields, each Dopplergram is mapped to a heliographic coordinate system and the resulting images are projected onto the spherical harmonics, following the method of Hathaway *et al.* (2000). This produces a two-dimensional power spectrum in spherical harmonic degree,  $\ell$ , and order,  $m$ . If necessary, contributions from instrumental calibration artifacts may be removed by setting the power at  $\ell < 11$ , for all  $m$ , equal to zero.

Additionally, the two-dimensional power spectrum is summed over  $m$  to produce a power spectrum in one-dimension (Figure 1). The strong feature seen peaking at around  $\ell = 125$  is caused by the presence of supergranules with a typical diameter of around 35 Mm.

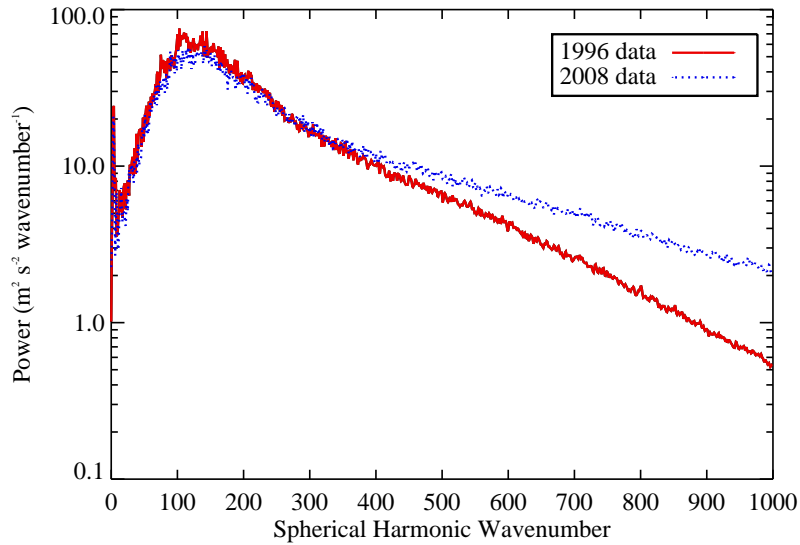


**Figure 1.** Examples of one-dimensional power spectra derived from processed Dopplergrams (solid line - 0000 UT, 25 May 1996; dotted line - 0000 UT, 4 March 2008). The supergranule feature that peaks at around  $\ell = 125$  dominates the spectrum. Power at low wavenumbers is related to instrument calibration artifacts. The reduction in power at high wavenumbers is due to the relative lack of features at that spatial scale, compared to supergranulation. Note that the reduction in power is steeper for 1996 than for 2008. This is caused by changes in defocusing between 1996 and 2008 (Korzennik *et al.*, 2004) that impacts the wavenumber domain above  $\ell \approx 300$ .

### 3. Data Analyses

#### 3.1. Supergranule Sizes

Supergranule sizes have been studied via analyses of magnetograms (Komm, 1995), Ca II K images (Hagenaar, 1997) and intensity maps (Meunier *et al.*, 2008). The method adopted in this paper to extract global averages of supergranule sizes from full-disk Dopplergrams is described by Hathaway *et al.* (2000) and examples of the spectra produced are shown in Figure 1.

Fits to the supergranule component of the convection spectrum can parameterize supergranule sizes. This process derives the wavenumber at which the peak occurs, which will provide a typical supergranule size estimation. Furthermore, a range of typical sizes can be determined by calculating the FWHM of the supergranule spectral peak.

We have analyzed the spectra from 1996 and 2008. For each year, spectra were produced for every Doppler image and averaged over the dataset to produce a spectrum with reduced noise and a smooth distribution. We performed fits to the supergranule peak, between the wavenumber range  $50 \leq \ell \leq 250$  of the convection spectrum, using a variety of fitting functions. By analyzing the residuals between the fit and the data between the given wavenumber range, we found that a modified Lorentzian, given by

$$f(\ell) = \left\{ \frac{\ell A}{[(\ell - \ell_0)^2 + \Gamma^2]} \right\}^2, \quad (1)$$

provides the best fit to the peak (Figure 2), as opposed to the Boltzmann and log-normal functions that were also tested, where  $\ell$  is the wavenumber, and  $A$ ,  $\ell_0$ , and  $\Gamma$  are the amplitude, peak wavenumber and width of the Lorentzian, respectively. A typical supergranule diameter,  $\lambda$ , may be derived from the peak wavenumber of the fit,  $\ell_{\text{peak}}$ , using

$$\lambda = \frac{2\pi R_{\odot}}{\ell_{\text{peak}}}, \quad (2)$$

which may also be used to determine a spatial range,  $\Delta\lambda$ , from the end values of the FWHM.

For the 1996 dataset, the peak wavenumber was determined to be  $\ell_{\text{peak}} = 122 \pm 1$ , with a FWHM of  $\Delta\ell = 155 \pm 3$ , corresponding to an average diameter of  $\lambda = 35.9 \pm 0.3$  Mm and a size range of 19.7–65.6 Mm ( $\Delta\lambda = 45.9$  Mm). The 2008 dataset gave a peak wavenumber of  $\ell_{\text{peak}} = 125 \pm 1$  and a FWHM of  $\Delta\ell = 164 \pm 5$ , corresponding to an average diameter of  $\lambda = 35.0 \pm 0.3$  Mm and a size range of 18.9–65.0 Mm ( $\Delta\lambda = 46.1$  Mm).

### 3.2. Supergranule Velocity Components

Below the surface, convecting material may be assumed to be rising vertically, carrying energy outward from the solar interior. Near the surface, where the

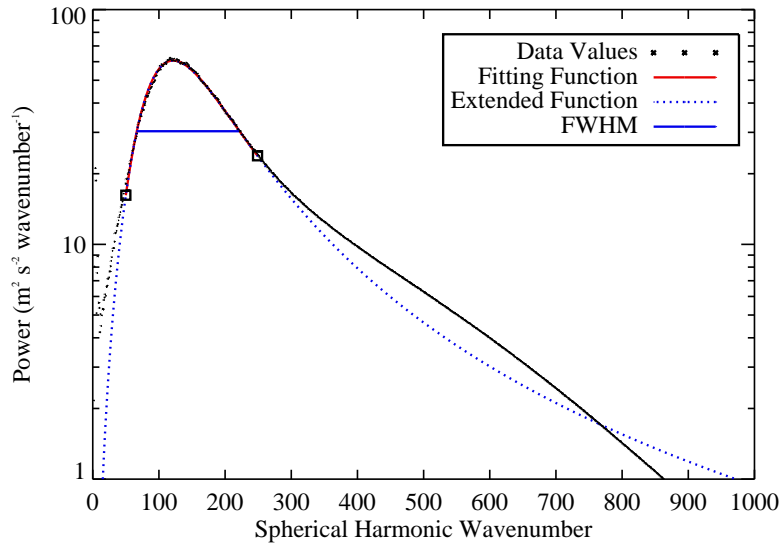


**Figure 2.** An averaged convection spectrum is fitted by a modified Lorentzian between  $50 \leq \ell \leq 250$ . The fit, performed within the range represented by the square symbols, provides both the wavenumber at which the peak occurs and the FWHM of the feature. For the 1996 dataset shown, these were found to be  $\ell_{\text{peak}} = 122 \pm 1$  and  $\Delta\ell = 155 \pm 3$ , respectively. For the 2008 dataset,  $\ell_{\text{peak}} = 125 \pm 1$  and  $\Delta\ell = 164 \pm 5$ .

material becomes convectively stable, the radial flow becomes a divergent, horizontal flow and the material spreads out over the surface from the center of the convection cell with the excess energy radiated to space. Where adjacent cells meet, their respective horizontal flows converge at their boundaries, becoming vertical downflows.

It is of interest to measure these velocity components as both flows play an important role in structuring the magnetic field. Radial flows tend to bring field lines to the surface, while horizontal flows advect the lines to the edges of the surface cells to produce structures such as those seen in the chromospheric network.

Hathaway *et al.* (2002) devised a method to extract the RMS velocity components by analyzing Dopplergrams from the 1996 MDI Dynamics Run. They derived typical values for radial and horizontal flow components of  $V_r = 29 \pm 2$  m s<sup>-1</sup> and  $V_h = 258 \pm 1$  m s<sup>-1</sup>, respectively. We have applied this analysis to

both the 1996 and 2008 MDI Dynamics Run data to compare typical values of these velocity components. The method is as follows.

Each Dopplergram is reduced to a heliocentric map of the supergranulation velocity as described in Section 2. Each pixel's velocity value is squared and the resulting array is binned into a set of 200 annuli centered on disk center at a heliocentric angular distance,  $\rho$ , from disk center. The average squared velocity in each annulus is then calculated. This process is repeated for each image in the data set and the average over the dataset for each annulus is taken. This produces a set of mean-squared velocity values,  $\overline{V^2(\rho)}$  at angular distance,  $\rho$ .

Using (Hathaway *et al.*, 2002),

$$\overline{V^2(\rho)} = \overline{V_r^2} + (\overline{V_h^2} - \overline{V_r^2}) \sin^2 \rho, \quad (3)$$

where  $V_r$  and  $V_h$  are the radial and horizontal velocity components, respectively, the mean-squared velocity values can then be plotted against  $\sin^2 \rho$ . It should be noted that, as well as  $V_r$ , the  $V_h$  component is limited to velocities directed along the line of sight; any horizontal component perpendicular to the line of sight does not contribute. Linearly fitting the data provides  $V_r$  and  $V_h$  from the intercept and gradient of the fit, respectively. The fit is applied out to  $\sin^2 \rho = 0.25$  ( $\rho = 30^\circ$ ) as, above this value, the data falls away due to limb effects. These methods were applied to both the 1996 and 2008 datasets and the results compared.

For 1996, the results derived were  $V_r = 24 \text{ m s}^{-1}$  and  $V_h = 278 \text{ m s}^{-1}$ , with a  $V_r/V_h$  ratio of 0.09, values similar to Hathaway *et al.* (2002). For 2008, the analysis produced  $V_r = 40 \text{ m s}^{-1}$  and  $V_h = 303 \text{ m s}^{-1}$  with a  $V_r/V_h$  ratio of 0.13, values notably greater than for 1996. However, this discrepancy is explained by the large amount of optical defocusing of MDI during 1996 (Korzennik *et al.*, 2004) which tends to blur the Doppler image and reduce the velocity value contained in each image pixel. The effect is also seen in the convection spectrum where the high wavenumber tail is lower in power for 1996 than for 2008 (Figure 1). We

have attempted to make the two datasets equivalent by; (1) smearing the 2008 Doppler images to reduce the pixel velocities and thus the spectral power at high wavenumbers; and (2) spectrally filtering the images of both 1996 and 2008 so that power at the high wavenumber tail does not contribute to the velocity analysis so removing the influence of defocusing.

Dopplergrams from 2008 underwent smearing to mimic the defocusing of the 1996 images. This was carried out on the original 15-min cadence images prior to the reduction process so that the artificial defocusing could be performed as near to the source of the images as possible. The smeared image is then processed as described in Section 2 and the respective convection spectrum compared to one from 1996. A two-dimensional Gaussian with a FWHM of 3.5 pixels smeared the images by an amount that resulted in spectra at high-wavenumbers very similar to those from 1996. The velocity analysis was then carried out on the smeared 2008 data with the linear fit applied out to  $\sin^2 \rho = 0.36$  ( $\rho \approx 37^\circ$ ), giving velocity components of  $V_r = 28 \pm 3 \text{ m s}^{-1}$  and  $V_h = 269 \pm 3 \text{ m s}^{-1}$  with a  $V_r/V_h$  ratio of  $0.11 \pm 0.01$ . For a similar fitting regime, for 1996 the values are  $V_r = 26 \pm 2 \text{ m s}^{-1}$  and  $V_h = 272 \pm 2 \text{ m s}^{-1}$  with a  $V_r/V_h$  ratio of  $0.11 \pm 0.01$ . However, comparing the two spectra at high wavenumbers exhibited noticeable differences in power which would still contribute to the velocity values, thus this method was deemed unsatisfactory for making a decent comparison of velocities between the two datasets.

The other method to equate the data sets and remove the influence of the defocusing is by selecting velocities within a limited range of the convection spectrum, notably around the supergranulation peak, thus suppressing the power at high wavenumbers (Figure 1). We have filtered the 1996 and 2008 reduced Doppler images with a log-normal distribution given by

$$F(\ell) = \frac{1}{\sigma \ell \sqrt{2\pi}} \exp \left[ \frac{-\ln^2(\ell/\mu)}{2\sigma^2} \right], \quad (4)$$

where  $\ell$  denotes the wavenumber, and  $\mu$  and  $\sigma$  are the mean and standard deviation of the variable, respectively. These latter parameters are adjusted so that the filter retains much of the power within the supergranule feature, but reduces power at very low wavenumbers (to remove any remaining instrumental artifacts) and at higher wavenumbers so to remove the discrepancy between the 1996 and 2008 spectra. For this study, the values used were,  $\mu = 136$  for 1996 and  $\mu = 139$  for 2008 to account for the shift in the mean peak between the two datasets as discussed in Section 3.1, while  $\sigma = 0.35$  for both years. The function was normalized by dividing through it by its maximum value.

We then performed the same analysis on these filtered images, but extending the linear fit out to  $\sin^2 \rho = 0.5$  ( $\rho = 45^\circ$ ) as the filtering tends to reduce the center-to-limb effects. For 1996 (Figure 3a), we get  $V_r = 7.6 \pm 1.4 \text{ m s}^{-1}$  and  $V_h = 139 \pm 1 \text{ m s}^{-1}$  with a  $V_r/V_h$  ratio of  $0.05 \pm 0.01$ . For 2008 (Figure 3b), we find  $V_r = 7.5 \pm 1.6 \text{ m s}^{-1}$  and  $V_h = 141 \pm 1 \text{ m s}^{-1}$  with a  $V_r/V_h$  ratio of  $0.05 \pm 0.01$ .

### 3.3. Supergranule Lifetimes

Convection cells have a limited lifetime. While it is observed that granules last much less than an hour (Hirzberger *et al.*, 1999), supergranules decay after about 24–48 h (Duvall, 1980) and giant cells can survive up to a few solar rotations (Beck *et al.*, 1998). Analyzing a time-series of Doppler velocity images, it can be seen that the patterns change with time as they move across the solar disk due to rotation. By following the rotation, correlation methods can be used to track the pattern and determine its decay rate.

Our correlation method is an adaptation of the one used by Hathaway *et al.* (2006) to study the superrotation of supergranules. After remapping to heliographic coordinates, we select a strip of velocity data containing a supergranule Doppler velocity pattern from the time-series. On each subsequent heliographic

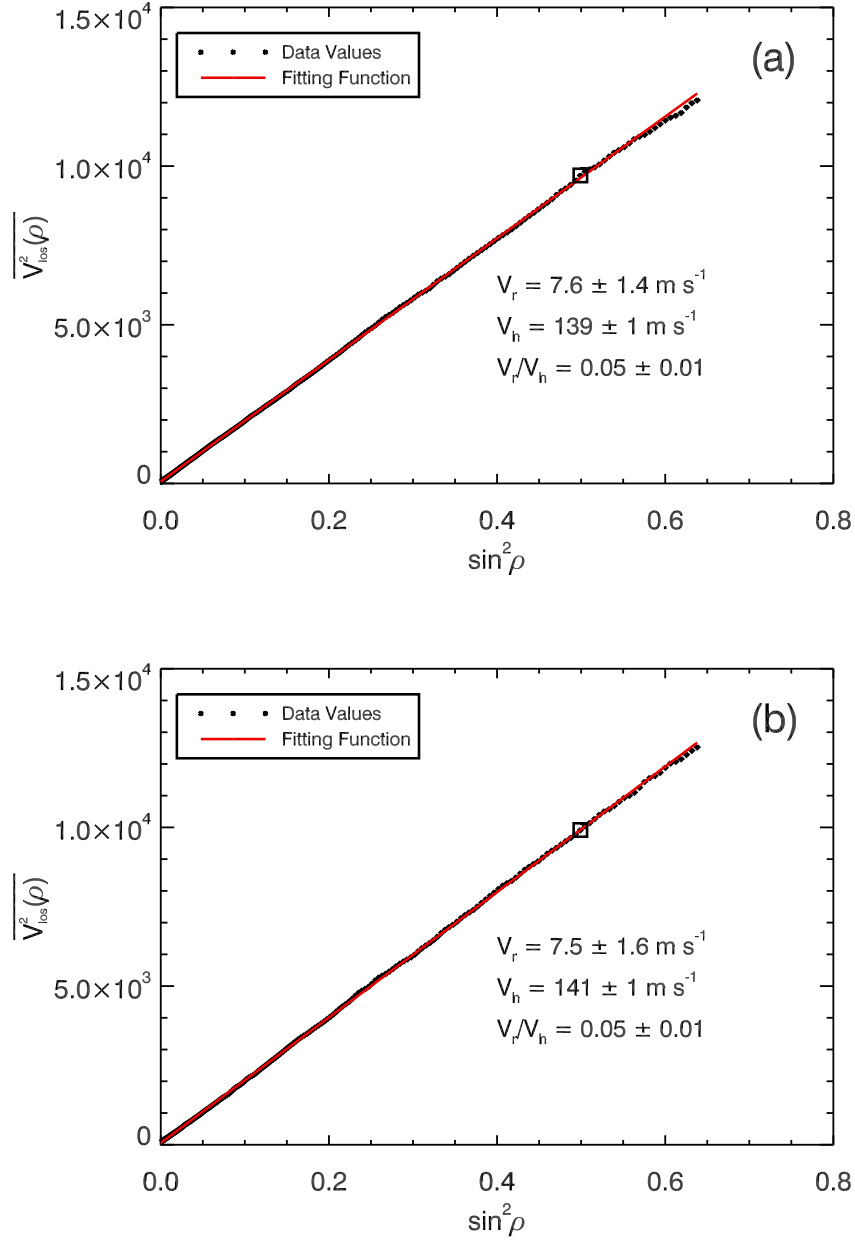


**Figure 3.** Plots of mean-squared line-of-sight velocity,  $\overline{V_{\text{los}}^2(\rho)}$ , as a function of  $\sin^2 \rho$ , where  $\rho$  is the heliocentric angular distance from disk center, averaged over a whole dataset for 1996 (a) and 2008 (b). The linear fits were applied out to  $\sin^2 \rho = 0.5$ , signified by the square symbol. Above this value, limb effects begin to non-linearly affect the data. For 1996 (a), we get  $V_r = 7.6 \pm 1.4 \text{ m s}^{-1}$  and  $V_h = 139 \pm 1 \text{ m s}^{-1}$  with a  $V_r/V_h$  ratio of  $0.05 \pm 0.01$ . For 2008 (b), we find  $V_r = 7.5 \pm 1.6 \text{ m s}^{-1}$  and  $V_h = 141 \pm 1 \text{ m s}^{-1}$  with a  $V_r/V_h$  ratio of  $0.05 \pm 0.01$ . As the horizontal velocity provides most of the power, this is the best parameter with which to make inter-year comparisons.

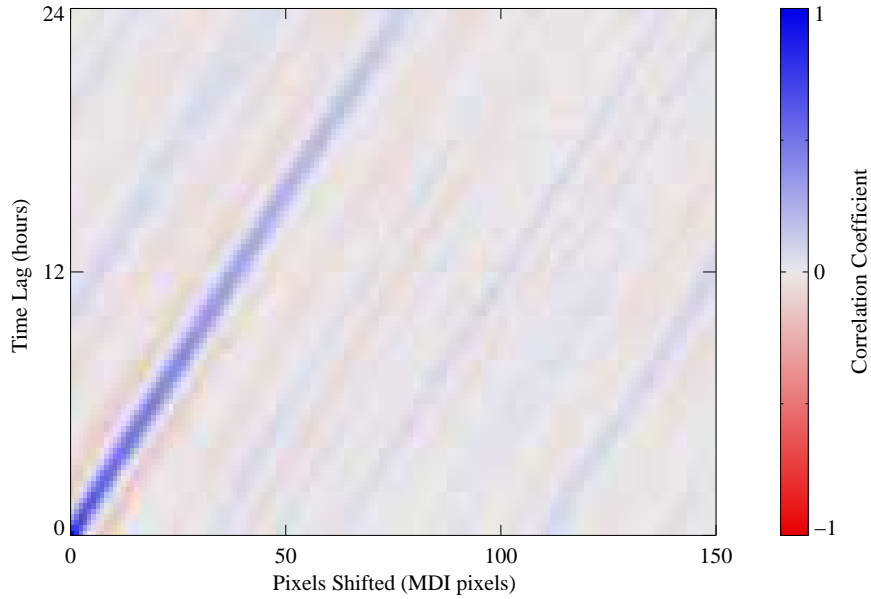


**Figure 4.** A correlation array for MDI Day 5541 (4 March 2008) dataset. The diagonal path from the bottom left corner shows decaying positive correlation tracking the evolution of the original supergranule Doppler pattern through subsequent images. After using Radon transforms to produce a mask that isolates the correlation path, calculating the peak correlation at each time-lag provides a dataset of decaying correlation values for a given day.

image, another strip of data the same size as the original strip is moved pixel by pixel longitudinally across the image and the correlation between the shifted strip and the original strip calculated. This is done for every image in the time series. The strips are 300 pixels in length by 50 pixels in height corresponding to  $\approx 27^\circ$  in longitude by  $\approx 9^\circ$  in latitude. They are extracted near the equator (centered on  $\approx 4.5^\circ\text{N}$ ) to reduce perspective effects and positioned in the western hemisphere so that correlations are not affected by the sign change in the velocity values as the tracked patterns cross the central meridian. The result is that for every 15-min image, a one-dimensional array of correlation coefficients for every pixel shifted is produced. The result is a two-dimensional (pixel-shift vs. time-lag) array of correlation coefficients (Figure 4).

The decrease in the correlation coefficient with respect to the original image can be analyzed to follow the decay of a selected convection pattern. The cor-

relation values can be tracked in time, beginning from the bottom left corner of the array and following a track of correlation values. It can be seen from Figure 4 that the correlation follows a diagonal path of positive correlation from the bottom-left of the array. This shows that the convection pattern moves, due to rotation, across the image in time as it decays. A Radon transform can be used to select and isolate features within images by parameterizing straight lines in image space to corresponding points in Radon space defined by the gradient and intercept of the image lines. Performing a Radon transform on the correlation array and selecting a region in Radon space at intercept values on either side of zero at the gradient value of the diagonal track can be used to isolate the track. These values can be used to produce an array in Radon space that, when inversely transformed, produces a mask that can be overlaid over the correlation array to select the diagonal track and mask out all other correlation values. The maximum at each time lag in the correlation of the track can then be found. The result is a correlation coefficient for each time-lag.

An alternative method for following the correlation track is to search for a local maximum within a limited pixel range ( $\pm 10$ ) around the position of the maximum for the previous time-lag. This maximum would give the correlation coefficient for that time lag. Both of these methods produced identical results, as expected, and helped to isolate the correlation maximum for each time-lag, while avoiding any false maxima that might otherwise have been inadvertently selected.

It is found that the extracted correlation coefficient,  $C(\Delta\tau)$  decays exponentially with lag-time,  $\Delta\tau$ . The slope of a straight line fitted to a log-linear plot ( $\ln C[\Delta\tau]$  vs.  $\Delta\tau$ ) gives the decay coefficient. The inverse of this slope provides the  $1/e$  lifetime,  $\tau_{1/e}$ , of the pattern.

This process was performed for each day within both datasets. A strip extracted from the first image within a given day is correlated with a similar strip moved over the subsequent set of 95 images. Correlation coefficient vs. time-lag

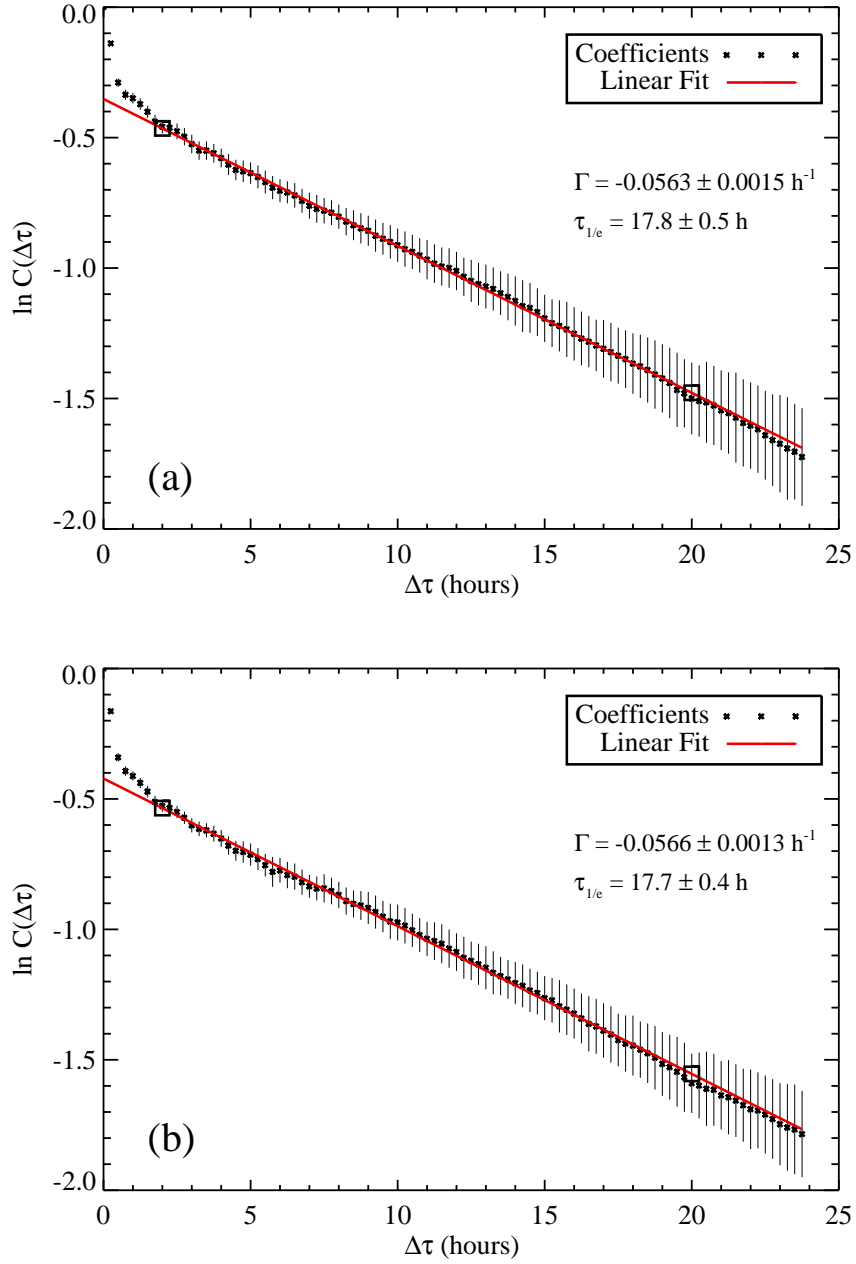


**Figure 5.** Correlation coefficients,  $C(\Delta\tau)$ , at each time-lag,  $\Delta\tau$ , are extracted from the correlation path shown in Figure 4 for each day and averaged over the whole year's dataset to produce the  $C(\tau)$  vs  $\tau$  data shown here; (a) and (b) show the respective 1996 and 2008 data averages and fits. The data is linearly fitted and the gradient provides the decay coefficient,  $\Gamma$ , from which the 1/e lifetime,  $\tau_{1/e}$ , is derived. In both figures, the points show the data that is fitted by the solid line between a given time range indicated by the square boxes. For both 1996 and 2008 the lifetimes are determined, from the decay coefficient,  $\Gamma$ , to be 18 h.

data is averaged over the entire dataset and a linear fit produced. This fit provides the the decay coefficient and 1/e lifetime for each dataset (Figure 5). The faster-than-exponential decay at early times in both plots is due to the presence of granules with lifetimes of 1-2 h (D.H. Hathaway, private communication).

The 1996 dataset provides an average decay coefficient,  $\Gamma = 5.63 \pm 0.15 \times 10^{-2} \text{ h}^{-1}$  or  $\tau_{1/e} = 17.8 \pm 0.5 \text{ h}$ . For 2008, the average decay coefficient,  $\Gamma = 5.66 \pm 0.13 \times 10^{-2} \text{ h}^{-1}$  or  $\tau_{1/e} = 17.7 \pm 0.4 \text{ h}$ .

#### 4. Discussion, Conclusion and Future Work

A summary of the parameters compared between 1996 and 2008 is given in Table 1. An additional parameter is the average number of supergranules on the solar disk during each year which is calculated using

$$N_{\text{SG}} = \frac{4\pi R_{\odot}^2}{\pi (\lambda/2)^2} = 16 \left( \frac{R_{\odot}}{\lambda} \right)^2, \quad (5)$$

where  $R_{\odot}$  is the solar radius and  $\lambda$  is the average supergranule diameter. It is found that there is a 5% increase in number of supergranules on the solar disk from 1996 to 2008.

**Table 1.** Table comparing supergranule parameters from 1996 and 2008.

Parameter	Symbol	Units	1996	2008
Spectral peak wavenumber	$\ell_{\text{peak}}$		$122 \pm 1$	$125 \pm 1$
Spectral peak FWHM	$\Delta\ell$		$155 \pm 3$	$164 \pm 4$
Supergranule diameter	$\lambda$	Mm	$35.9 \pm 0.3$	$35.0 \pm 0.3$
Radial velocity	$V_r$	$\text{m s}^{-1}$	$7.6 \pm 1.4$	$7.5 \pm 1.6$
Horizontal velocity	$V_h$	$\text{m s}^{-1}$	$139 \pm 1$	$141 \pm 1$
1/e Lifetime	$\tau_{1/e}$	h	$17.8 \pm 0.5$	$17.7 \pm 0.4$
Number of SGs	$N_{\text{SG}}$		6005	6318

By averaging all the power spectra derived from all the Dopplergrams in both 1996 and 2008, respectively, followed by a calculation of the peak wavenumber of the supergranule feature, the typical supergranule size can be estimated (Section 3.1). Comparing the diameter values listed in Table 1, on average supergranules were smaller in 2008 than in 1996, despite the size range itself being approximately equal.

As the horizontal velocities are consistently at least ten times the values of the radial components, they provide most of the power that is seen within the convection spectrum and are thus the best parameter with which to make inter-year comparisons. However, the high-wavenumber power discrepancy between the two datasets make any direct velocity comparisons difficult, due to different levels of instrument defocus during the respective observation times.

To equalize the data, the Dopplergrams from each year were spectrally filtered with a log-normal distribution. This maintained the power within the supergranule feature while suppressing the power at higher wavenumbers that is influenced by defocusing. The process described in Section 3.2 was then repeated for both filtered datasets. As the same process was applied to both datasets, providing suppression of the problematic high wavenumber region, it is felt that this method provides a reliable inter-year comparison. The horizontal velocity values listed in Table 1 suggest that the horizontal flows are marginally stronger during 2008 than during 1996.

Strips of data near the solar equator were taken from a base Dopplergram and cross-correlated with strips in subsequent Dopplergrams within each day contained within each dataset. The natural logarithm of the correlation values at each time-lag between the two correlated strips was calculated and averaged over all days. This provided a dataset that could be linearly fitted, the gradient of which provided the decay coefficient from which the  $1/e$  decay time of the supergranule pattern could be calculated. Assuming the  $1/e$  decay times provide

a decent estimate of the supergranule lifetimes, as listed in Table 1, supergranule lifetimes are no different between 2008 and 1996.

To conclude, while supergranule lifetimes are the same between 2008 and 1996, their sizes tend to be larger during 1996, while their horizontal flows seem to be stronger during 2008. However, the differences seen are not substantial enough to suggest that the convection zone was behaving any differently during the two epochs to reflect the dramatic differences observed within the sunspot number. This is in contrast to other work such as the analyses of Howe *et al.* (2009), who saw distinct differences within torsional oscillation maps covering both solar minima.

To better determine whether the observed differences do actually correlate to differences within the global field between the two years requires the results to be placed into the larger context of data gathered around solar maximum where the magnetic field strength is quite different to that at minimum. An analysis of data from 2009 would also provide better comparisons between minima as the activity during 1996 and 2009 appears to be of similar phase within the solar cycle. These future analyses will improve our picture of the interaction between the magnetic field and convection. Comparisons may also be made with other research into convection cell characteristics throughout a solar cycle such as the supergranule size measurements made by Meunier and Roudier (2007) and to analyses of cell sizes, their relationship to velocities inside the cell and intensity variations across the cell by Meunier *et al.* (2008).

Further studies will apply methods similar to those described in this paper to individual Dopplergrams and present a statistical analysis of the time-dependent parameters investigated in this paper. The work will be extended to study characteristics of supergranule-influenced features visible in MDI magnetograms, Ca II K images of the solar chromosphere using the instruments such as the Precision Solar Photometric Telescope and H $\alpha$  observations. Supergranule ve-

locity comparisons may also be made by extracting their component values using Time-Distance Helioseismology methods (Duvall *et al.*, 1993).

The studies of convection cells at cycle minimum within these many regimes of observation may also assist in quantifying hemispheric asymmetries that may exist. A number of similar studies have been made (for example, Osherovich *et al.*, 1999) and it would be of interest to observe and compare any hemispheric differences that may exist within each of the characteristics studied during the periods of solar minima covered in this paper.

With the launch of the Helioseismic Magnetic Imager (HMI) instrument (J. Schou, private communication) aboard the Solar Dynamics Observatory (SDO) satellite (W.D. Pesnell, private communication) in February 2010, the spatial range of the studies provided here may be extended by the enhanced spatial resolution of HMI. Observations made via the high-resolution mode of MDI provide convection spectra that clearly show a feature due to granulation (Hathaway *et al.*, 2000). SDO/HMI offers the opportunity to study granulation at the same resolution as supergranulation and make comparisons of convection cell characteristics throughout this extended convection spectrum.

**Acknowledgements** This research was supported by an appointment to the NASA Postdoctoral Program at NASA Goddard Space Flight Center, administered by Oak Ridge Associated Universities through a contract with NASA via the Solar Dynamics Observatory. SOHO is a project of international cooperation between ESA and NASA. The authors extend their gratitude to John Beck of Stanford University for producing the de-rotated Dopplergram datasets. We also thank the referee for the constructive comments.

## References

- Beck, J.G., Schou, J.: 2000, *Solar Phys.* **193**, 333.  
Beck, J.G., Duvall, T.L. Jr., Scherrer, P.H.: 1998, *Nature* **394**, 653.  
DeRosa, M.L., Toomre, J.: 2004, *Astrophys. J.* **616**, 1242.  
Duvall, T.L. Jr.: 1980, *Solar Phys.* **66**, 213.

- Duvall, T.L. Jr., Jeffries, S.M., Harvey, J.W., Pomerantz, M.A.: 1993, *Nature* **362**, 430.
- Hart, A.B.: 1956, *Mon. Not. Roy. Astron. Soc.* **116**, 38.
- Hagenaar, H.J., Schrijver, C.J., Title, A.M.: 1997, *Astrophys. J.* **481**, 988.
- Hathaway, D.H.: 1987, *Solar Phys.* **108**, 1.
- Hathaway, D.H.: 1988, *Solar Phys.* **117**, 1.
- Hathaway, D.H.: 1992, *Solar Phys.* **137**, 15.
- Hathaway, D.H., Beck, J.G., Bogart, R.S., Bachmann, K.T., Khatri, G., Pettito, M., Han, S., Raymond, J.: 2000, *Solar Phys.* **193**, 299.
- Hathaway, D.H., Beck, J.G., Han, S., Raymond, J.: 2002, *Solar Phys.* **205**, 28.
- Hathaway, D.H., Williams, P.E., Cuntz, M.: 2006, *Astrophys. J.* **644**, 598.
- Hirzberger, J., Bonet, J.A., Vázquez, M., Hanslmeier, A.: 1999, *Astrophys. J.* **515**, 441.
- Howe, R., Christensen-Dalsgaard, J., Hill, F., Komm, R., Schou, J., Thompson, M.J.: 2009, *Astrophys. J. Lett.* **701**, 87.
- Käpylä, P.J., Korpi, M.J., Tuominen, I.: 2006, *Astrophys. J.* **327**, 884.
- Komm, R.W., Howard, R.F., Harvey, J.W.: 1995, *Solar Phys.* **158**, 213.
- Korzennik, S.G., Rabello-Soares, M.C., Schou, J.: 2004, *Astrophys. J.* **602**, 481.
- Leighton, R.B., Noyes, R.W., Simon, G.W.: 1962, *Astrophys. J.* **135**, 474.
- Lisle, J.P., Rast, M.P., Toomre, J.: 2004, *Astrophys. J.* **608**, 1167.
- Matloch, L., Cameron, R., Schmitt, D., Schüssler, M.: 2009, *Astron. Astrophys.* **504**, 1041.
- Meunier, N., Roudier, T.: 2007, *Astron. Astrophys.* **466**, 691.
- Meunier, N., Roudier, T., Rieutord, M.: 2008, *Astron. Astrophys.* **488**, 1109.
- Miesch, M.S., Elliot, J.R., Toomre, J., Clune, T.L., Glatzmaier, G.A., Gilman, P.A.: 2000, *Astrophys. J.* **532**, 593.
- November, L.J., Toomre, J., Gebbie, K.B., Simon, G.W.: 1981, *Astrophys. J. Lett.* **245**, 123.
- Osherovich, V.A., Fainberg, J., Fisher, R.R., Gibson, S.E., Goldstein, M.L., Guhathakurta, M., Siregar, E.: 1999, In: Habbal, S.R., Esser, R., Hollweg, J.V., Isenberg P.A. (eds.), *Solar Wind Nine, AIP Conf. Proc.* **471**, 721.
- Pevtsov, A.A., Neidig, D.: 2005, In: Sunkarasubramaniam, K., Penn, M., Pevtsov, A. (eds.), *Large-Scale Structures and their Role in Solar Activity, ASP Conf. Ser.* **346**, 593.
- Rast, M.P.: 2003, In: Sawaya-Lacoste, H. (ed.), *Proc. SOHO 12 / GONG+ 2002, Local and Global Helioseismology: the Present and Future, ESA SP-517*, 163.
- Rieutord, M., Meunier, N., Malherbe, J.M., Rincon, F.: 2000, *Astron. Astrophys.* **357**, 1063.
- Rieutord, M., Meunier, N., Roudier, T., Rondi, S., Beigbeder, F., Parès, L.: 2009, *Astron. Astrophys.* **479**, 17.
- Scherrer, P.H., Bogart, R.S., Bush, R.I., Hoeksema, J.T., Kosovichev, A.G., Schou, J., et al.: 1995, *Solar Phys.* **162**, 129.

Simon, G.W., Weiss, N.O.: 1968, *Z. Astrophys.* **69**, 435.

Stein, R.F., Nordlund, Å.: 2000, *Solar Phys.* **192**, 91.

Williams, P.E., Cuntz, M.: 2009, *Astron. Astrophys.* **505**, 1265.